Article

Enhancing Volumetric Stability of Metakaolin-Based Geopolymer Composites with Organic Modifiers WER and SCA

Mo Zhang [1], Yongquan Zang [1] and Lingyan Shan [2],*

1   School of Civil and Transportation Engineering, Hebei University of Technology, 5340 Xiping Road, Tianjin 300401, China; mozhang@hebut.edu.cn (M.Z.); 202121601059@stu.hebut.edu.cn (Y.Z.)
2   Fundamental Research Innovation Center, Research Institute of Highway Ministry of Transport, 8 Xitucheng Road, Beijing 100088, China
*   Correspondence: ly.shan@rioh.cn

Abstract: Shrinkage during hardening and curing is one of the largest challenges for the widespread application of metakaolin-based geopolymers (MKGs). To solve this problem, a silane coupling agent (SCA) and waterborne epoxy resin (WER) were used to synthesize MKG composites. The individual and synergistic effects of the SCA and WER on chemical, autogenous, and drying shrinkage were assessed, the modification mechanisms were investigated by microstructural characterization, and shrinkage resistance was evaluated by the chloride ion permeability of MKG composite coatings. The results showed that the SCA and WER significantly decreased the chemical shrinkage, autogenous shrinkage, and drying shrinkage of the MKG, with the highest reductions of 46.4%, 131.2%, and 25.2% obtained by the combination of 20 wt% WER and 1 wt% SCA. The incorporation of the organic modifiers densified the microstructure. Compared with the MKG, the total volume of mesopores and macropores in MKG-WER, MKG-SCA, and MKG-WER-SCA decreased by 11.5%, 8.7%, and 3.8%, respectively. In particular, the silanol hydrolyzed from the SCA can react with the opened epoxy ring of the WER and the aluminosilicate oligomers simultaneously to form a compact network and resist shrinkage during the hardening and continuous reaction of the geopolymer. Furthermore, the apparently lowered chloride ion diffusion coefficient of concrete (i.e., reduction of 51.4% to 59.5%) by the WER- and SCA-modified MKG coatings verified their improved shrinkage resistance. The findings in this study provide promising methods to essentially solve the shrinkage problem of MKGs at the microscale and shed light on the modification mechanism by WERs and SCAs, and they also suggest the applicability of MKG composites in protective coatings for marine concrete.

Keywords: metakaolin-based geopolymer; chemical shrinkage; autogenous shrinkage; drying shrinkage; organic modification

1. Introduction

Geopolymers are a type of cementitious material synthesized through the alkali activation of aluminosilicate materials, such as metakaolin [1], granulated blast furnace slag [2], steel slag [3], etc. Due to the reuse capability of industrial by-products and low carbon emissions of the production process, geopolymers have received wide research interest [4]. In recent years, the applicability of geopolymers as protective coating materials has been increasingly investigated due to their high toughness [5], high thermal stability [6], good corrosion resistance [7], and water impermeability [8]. A metakaolin-based geopolymer (MKG) coating presented excellent resistance to seawater corrosion and high adhesion strength to concrete and steel substrates [9], while the intrinsic shrinkage nature can induce serious cracking problems and limit the application of MKGs [10–12]. High shrinkage gave rise to microcracks in the MKG coating and accelerated the intrusion and penetration of aggressive ions into the concrete, rendering the geopolymer coating functionally ineffective [13].

Many efforts have endeavored to reduce shrinkage cracking risks [14]. Incorporating shortcut fibers is one of the most widely applied methods, which controls the development and expansion of cracks during different types of shrinkage [15,16]. Al et al. revealed that steel fibers and glass fibers reduced the drying shrinkage of fly ash-based geopolymer composites by 16–24% after curing for 28 days [17]. Vilaplana et al. showed that 0.2 wt% of 3 mm carbon fibers (CFs) was sufficient to reduce the maximum strain of drying shrinkage to less than 1.5 mm/m [15]. However, the workability and mechanical strength of the geopolymer were significantly impacted by the dispersity and type of fiber [18,19]. At the same time, the fibers cannot participate in geopolymerization, and thus, they can barely reduce shrinkage at the microscale and essentially dissolve shrinkage problems [20,21]. Other studies have focused on modifications with liquid organic solvents, such as silane coupling agents (SCAs) and waterborne epoxy resins (WERs), to reduce the shrinkage of geopolymers. Liquid organic solvents could be evenly dispersed in the geopolymer gels, thus enhancing the compactness of the geopolymer and inhibiting the propagation of microcracks in the geopolymer [22]. Wang et al. found that the incorporation of an SCA reduced the drying shrinkage of MKGs by 18% after curing for 28 days [23]. Zhang et al. found that the incorporation of an SCA improved the compressive strength of an MKG by 14.99% and the flexural strength by 11.24%. The structure of the MKG became more compact, and the closed pore size was reduced from 13.16 nm to 8.11 nm [24]. The improved mechanical and shrinkage properties were likely to have resulted from the involvement of the SCA in the polymerization of the MKG, generating enriched N-A-S-H gels and thus refining the pore structure of the SCA-MKG composites [25]. Epoxy resin is another organic solvent that can be well dispersed in geopolymers [26]. In contrast to the bond strength of geopolymer gels, epoxy resin had a strong interaction with the inorganic matrix of the geopolymer, as epoxy resin molecules opened their rings during the cross-linking process and formed a dense network of hydrogen bonds with each other, thus improving the strength of the geopolymer [27,28]. Apriany et al. found that epoxy resin reduced the drying shrinkage of fly ash–slag-based geopolymer composites by 5.2–12.2% [29]. Du et al. found that the compressive strength of a metakaolin-granulated blast furnace slag geopolymer increased by 30% with the incorporation of 20 wt% epoxy resin [30]. The improvement of the mechanical properties and durability of geopolymers suggested the wide application of liquid organic solvent modification. However, the performance and underlying mechanisms of shrinkage reduction in geopolymers by incorporating multiple organic solvents have rarely been reported.

Due to the distinctive reaction processes and microstructures of geopolymers compared with ordinary Portland cement (OPC), the shrinkage mechanism of geopolymers is quite different from that of OPC [31]. For geopolymers, autogenous shrinkage is the volume reduction caused by the combined action of self-desiccation and chemical shrinkage without water transferring to the external environment [32]. Among them, self-desiccation is caused by the dissolution process of geopolymers, continuously consuming pore water in the capillary pores, thus leading to the development of pores inside the geopolymer and generating capillary pressure [33]. Chemical shrinkage is caused by the variation in the density of geopolymer products before and after geopolymerization [34]. Li et al. found that MKGs underwent three stages of chemical shrinkage, i.e., chemical shrinkage, chemical expansion, and chemical shrinkage again [35]. However, chemical shrinkage is less likely to occur during the hydration of cement because of the great toughness and particle skeleton of cement [36]. In an open environment, drying shrinkage is caused by the evaporation of water from the pore structure of the geopolymer [37], which can be much greater than that of OPC [38,39]. Therefore, autogenous shrinkage, chemical shrinkage, and drying shrinkage correspond to the volume changes in the geopolymer during dissolution, pre-hardening, and post-hardening processes, respectively. Under the combined effect of autogenous shrinkage, chemical shrinkage, and drying shrinkage, the macroscopic volume of the geopolymer changes, leading to tensile stresses, inhomogeneous deformations, and damaging cracks, which can seriously affect the mechanical properties of the geopolymer

and thus its durability [40]. By adding additives to suppress the change in the geopolymer volume during the different reaction times of the geopolymer, the shrinkage of the geopolymer can be significantly reduced, and the strength of the geopolymer can be increased. Yang et al. found that the reaction of geopolymers based on fly ash and metakaolin drove the pore fluids to the autogenous shrinkage sites and reduced the capillary stresses, and autogenous shrinkage showed a negative trend (i.e., expansion) before it became positive (shrinkage) [41]. Ruan et al. [42] found that the hydrophobic chemical groups introduced by polydimethylsiloxane (PDMS) and sodium methylsilicate (SMS) could be strongly bound to the geopolymer gel, giving the MKG a good water-repellent effect and thus reducing autogenous shrinkage by 91.1% and 41.8%, respectively. In terms of chemical shrinkage, PDMS improved the dispersion of the solid precursors, and SMS increased the alkalinity of the MKG, allowing the MKG to form a denser and more amorphous Si-rich gel, which reduced the chemical expansion of the MKG. Tian et al. [43] found that the addition of 5 wt% silicon acrylic (Si-A) reduced the drying shrinkage of fly ash- and slag-based geopolymers by 63.5%. This was due to the film formed by the Si-A polymer on the hydration products, which sealed the water in the geopolymer and prevented its evaporation. However, the existing studies only focus on the effects of organic solvent modification on the shrinkage of geopolymers. There are few studies on the effects of organic solvents on the whole reaction process of geopolymers, i.e., autogenous shrinkage, chemical shrinkage, and drying shrinkage [44].

As shown in Figure 1, a waterborne epoxy resin (WER), a silane coupling agent (SCA), and a mixture of the above two were used to synthesize an organically modified MKG to reduce shrinkage in this study. The influence of the individual addition and synergistic mixture of the WER and SCA on the chemical shrinkage, autogenous shrinkage, and drying shrinkage of the MKG was investigated. The modification mechanism of the WER, SCA, and WER-SCA on the shrinkage properties of the MKG was analyzed using microstructural characterization by scanning electron microscopy (SEM), energy-dispersive spectroscopy (EDS), Fourier-transform infrared spectroscopy (FTIR), X-ray diffraction (XRD), mercury intrusion porosimetry (MIP), and nuclear magnetic resonance (NMR). An appropriate reaction process among the WER, SCA, and MKG was proposed. Finally, the resistance of the WER-SCA-modified MKG coating to chloride ion penetration was evaluated by rapid chloride migration (RCM) tests to illustrate its applicability in marine protective coatings.
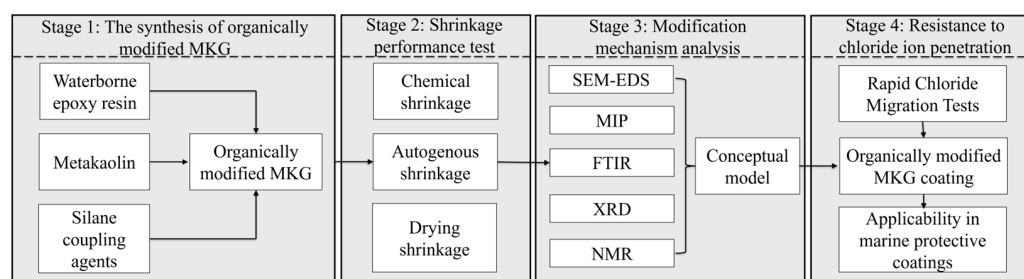

Figure 1. Research methodology of metakaolin-based geopolymer composites enhanced with organic modifiers WER and SCA.

2. Materials and Methods

2.1. Materials

Metakaolin (MK) with a mesh size of 1250 was provided by Jiaozuo Yukun Co., Ltd., in Jiaozuo, China. The average particle size of MK is 10 μm, and the specific surface area is 128,710 cm^2/g. The main chemical composition of MK is listed in Table 1, and the mineralogical properties are presented in the form of XRD patterns, as shown in Figure 2d. The alkaline activator solution used in the experiment was prepared with sodium metasilicate solution ($Na_2O \cdot 2SiO_2$, Na_2O/SiO_2 = 2.0, and a solid content of 42%) and 50 wt% sodium hydroxide (NaOH) solution. Deionized water was used throughout the experiments. E51 epoxy resin and the Q17 waterborne hardener (diethylenetriamine

(DETA) as the main ingredient) were selected as the main components to prepare the waterborne epoxy resin (WER). The n-Octyl triethoxy silane coupling agent (SCA) was selected as another type of organic modifier. E51 epoxy resin and the Q17 waterborne hardener were purchased from Yingyi Environmental Protection Technology Co., Ltd. in Weifang, China, and the silane coupling agent was purchased from Nanjing Feiteng Technology Co., Ltd., in Nanjing, China. The chemical structures of E51 epoxy resin, the SCA, and DETA are shown in Figure 2.

Table 1. Chemical composition of metakaolin.

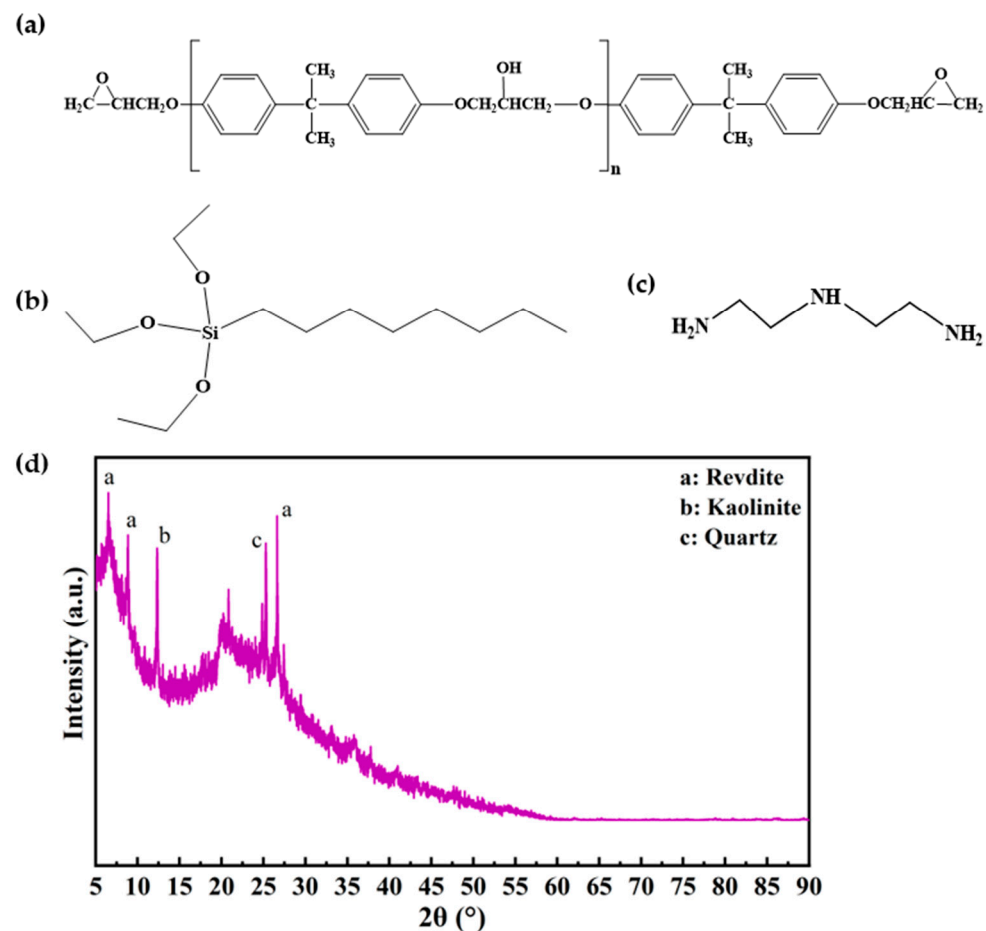| Metakaolin	SiO_2	Al_2O_3	TiO_2	Fe_2O_3	Na_2O	CaO	K_2O	MgO
Chemical Composition (wt%)	49.67	42.54	2.14	1.32	0.68	0.19	0.18	0.14

Figure 2. The chemical structures of (**a**) E51 epoxy resin, (**b**) the n-Octyl triethoxy SCA, and (**c**) DETA and (**d**) the XRD pattern of metakaolin.

2.2. Sample Preparation

The mix proportions of all MKG sample sets in this experiment are listed in Table 2 and were determined on the basis of previous studies [45,46]. A 50 wt% NaOH solution was prepared 24 h in advance and cooled to room temperature. The 50 wt% NaOH solution and $Na_2O \cdot SiO_2$ solution were mixed in a volume ratio of 5:1 to obtain the alkali activator solution. MK and the alkali activator solution were mixed for 3 min to obtain an MKG paste using a cement mortar mixer. At the same time, the waterborne curing agent Q17 and E51 epoxy resin were mixed in a mass ratio of 5:3 to obtain the waterborne epoxy resin (WER). For the WER-modified MKG (MKG-WER), the WER was mixed with the MKG paste in a mass ratio of 20%. The SCA was mixed with the MKG paste at a mass ratio of 1%

by direct dropping for the SCA-modified MKG (MKG-SCA). For the SCA-WER-modified MKG (MKG-WER-SCA), the SCA was slowly mixed with fresh MKG-WER paste at a mass ratio of 1% and stirred for 3 min. The prepared MKG and MKG-WER coatings are shown in Figure 3.

Table 2. Material compositions of organic-liquid-modified geopolymer.

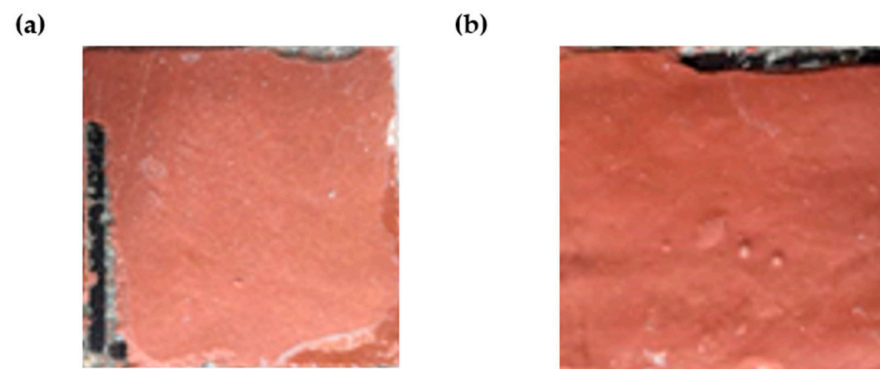| Sample	Metakaolin (g)	Na$_2$O·2SiO$_2$ (mL)	50 wt% NaOH (mL)	E51 Epoxy Resin (g)	Q17 Hardener (g)	SCA (g)
MKG	100	90	18	-	-	-
MKG-WER	100	90	18	32.9	19.8	-
MKG-SCA	100	90	18	-	-	2.6
MKG-WER-SCA	100	90	18	32.9	19.8	3.2

(a)   **(b)**

Figure 3. (**a**) MKG coating and (**b**) MKG–WER coating on cement concrete.

2.3. Testing Program

2.3.1. Drying Shrinkage Test

According to the Chinese standard GB/T 50082-2009 [47], 25 mm × 25 mm × 280 mm prism specimens were prepared and demolded after sealed curing for 24 h. The lengths of the specimens along the longitudinal axis were determined with a BC-300d bench comparator, with an accuracy of 0.001 mm. The specimens were cured in sealed bags at room temperature for 7 days. The first readings were recorded immediately after demolding, and then the daily length changes of the specimens were recorded to calculate the drying shrinkage.

2.3.2. Chemical Shrinkage Test

According to the ASTM standard C1608-2017 [48], dilatometry was used to measure the chemical shrinkage of the MKG, MKG-WER, MKG-SCA, and MKG-WER-SCA. The prepared pastes were injected into vials to a height of 7 mm. The paste level was then sealed with droplets of vegetable oil, and the vial was plugged using a rubber stopper with a graduated capillary tube inserted through it. The level of the vegetable oil in the graduated tube was within the graduation line. The vials were left to stand in a water bath to maintain the temperature at 23 °C. The initial readings of the bottom of the meniscus in the capillary tube were recorded after 1 h of curing, and then the level changes (hi) in the glass tube were recorded every hour for the first 8 h and every day thereafter. Chemical shrinkage was calculated according to Equation (1) [48]:

$$S_i = \frac{(h_i - h_0)}{m_c} \tag{1}$$

where S_i is the chemical shrinkage value in mL/g; h_0 is the initial height of the liquid level in the scale tube in mL; h_i is the change in the liquid level in the capillary tube in mL; and m_c is the mass of the pastes in the vials in g.

2.3.3. Autogenous Shrinkage Test

The autogenous shrinkage of four types of geopolymer composite pastes was measured continuously over a period of 7 days according to the ASTM standard C1698-2009 (2014) [49]. The prepared geopolymer composite paste was filled into a corrugated tube, of which the length change was monitored automatically with a digital gauge every hour from the final setting time (i.e., 6.5 h, 4 h, 6 h, and 3.5 h for MKG, MKG-SCA, MKG-WER, and MKG-WER-SCA, respectively) until the 24th h, and then every day for the following 6 days. Autogenous shrinkage was calculated according to Equations (2) and (3) [49]:

$$L_0 = L_{ref} + R_t - 2L_{plug} \tag{2}$$

$$\varepsilon = \frac{R_t - R_i}{L_0} \times 10^6 \tag{3}$$

where L_0 is the initial length of the sample measured at the final setting time in mm; L_{ref} is the length of the reference rod in mm; R_t is the reading of the dial gauge at each measurement moment in mm; L_{plug} is the length of one stopper plugged in one end of the corrugated tube in mm; ε is the autogenous shrinkage in μm/mm; and R_i is the dial gauge reading at the final setting time in mm.

2.3.4. Microstructural Characterization

The microstructural evolution of the four types of geopolymer composites was characterized using an S4800 scanning electron microscope at an accelerating voltage of 5 kV, and EDS was conducted to determine the chemical compositions of the resins and geopolymer gels. The pore size distribution and pore volume of the composites were measured by mercury intrusion porosimetry with a Micromeritics Autopore IV, and cubic specimens of about 27 mm^3 were used. The bonding structure of the specimens was characterized by a TENSOR 27 FTIR device in the wavelength range from 600 cm^{-1} to 4000 cm^{-1}. The mineral composition of the specimens was determined using a Smartlab 9KW XRD diffractometer with CuKα radiation at a voltage of 40 kV and a current of 100 mA. The scan rate was 6°/min from 5° to 40° (2θ) at 0.02/step. The chemical reaction between the organic modifier and the geopolymer was characterized by solid-state 27Al and ^{29}Si nuclear magnetic resonance (NMR) using a Bruker 400M NMR spectrometer with a probe diameter of 4 mm and a MAS spin rate of 10 KHz. The parameters of ^{27}Al NMR and ^{29}Si NMR were as follows:

For ^{27}Al MAS NMR, the resonance frequency was 104.26 MHz, single-pulse sampling was adopted, the pulse width was 0.97 μs, the relaxation delay time was 1 s, the number of scans was 800 times, and the chemical shift was referenced to aqueous $NaAlO_2$.

For ^{29}Si MAS NMR, the resonance frequency was 79.49 MHz, single-pulse sampling was adopted, the pulse width was 4.97 μs, the relaxation delay time was 5 s, the number of scans was 512 times, and the chemical shift was referenced to tetramethyl orthosilicate at 0 ppm.

2.3.5. Rapid Chloride Migration Test

According to the Chinese standard GB/T 50082-2009 [47], the chloride ion penetration resistance of geopolymer coatings was measured by the rapid chloride migration (RCM) test. Cylindrical concrete specimens with a size of φ100 mm × 50 mm after curing for 14 days were used for this experiment. A 2~3 mm thick geopolymer paste coating was applied to the top and bottom surfaces of the specimens. The sides of the specimens were coated with a petroleum wax sealant and then cured at room temperature for 7 days. During the test, the applied voltage was set to 30 V to record the initial current. Based on the initial current, the applied voltage was adjusted according to the relationship between the initial current and voltage in Table 3, and a new initial current and voltage were recorded. At the end of the assigned test duration, the initial and final temperatures of the anode solution were recorded by electrocouples, and the duration of the experiment was recorded. The diffusion coefficient of the chloride ion was calculated according to Equation (4) [47]:

$$D_{RCM} = \frac{0.0239 \times (273 + T)L}{(U - 2)t} \left(X_d - 0.0238\sqrt{\frac{(273 + T)LX_d}{U - 2}} \right) \qquad (4)$$

where D_{RCM} is the chloride ion migration coefficient in $\times 10^{-12}$ m^2/s; U is the absolute value of the applied voltage according to Table 3 in V; T is the average value of the initial and final temperature of the anode solution in °C; L is the thickness of the geopolymer specimens in mm; X_d is the average value of the chloride ion penetration depth in mm; and t is the test duration in h.

Table 3. The relationship between the initial current, voltage, and test time [47].

Initial Current (I_{30V}/mA)	Applied Voltage (U/V)	Possible New Initial Current (I_0/mA)	Duration of Test (t/h)
$I_0 < 5$	60	$I_0 < 10$	96
$5 \leq I_0 < 10$	60	$10 \leq I_0 < 20$	48
$10 \leq I_0 < 15$	60	$20 \leq I_0 < 30$	24
$15 \leq I_0 < 20$	50	$25 \leq I_0 < 35$	24
$20 \leq I_0 < 30$	40	$25 \leq I_0 < 40$	24
$30 \leq I_0 < 40$	35	$35 \leq I_0 < 50$	24
$40 \leq I_0 < 60$	30	$40 \leq I_0 < 60$	24

3. Results and Discussion

3.1. Chemical, Autogenous, and Drying Shrinkage

The drying shrinkage, chemical shrinkage, and autogenous shrinkage of the WER-, SCA-, and SCA-WER-modified MKG composites were tested and are illustrated in Figure 4. As shown in Figure 4a, the drying shrinkage of the MKG and MKG composites increased sharply in the first 10 days, then slowed down, and gradually tended to be stable on the 21st day. The drying shrinkage of MKG-SCA, MKG-WER, and MKG-WER-SCA was much lower than that of the MKG. In particular, the shrinkage of MKG-WER-SCA was even lower than that of MKG-SCA and MKG-WER. Compared to the MKG, the drying shrinkage of MKG-SCA, MKG-WER, and MKG-WER-SCA on the 28th day decreased by 24.5%, 23.5%, and 25.2%, respectively. Since only a small amount of water existed in the form of bonding water in geopolymers, a large amount of unbound water or free water evaporated during the curing process, resulting in large drying shrinkage in the early stage. Consistently, the chemical shrinkage of all four samples developed rapidly in the early stage and then became slower after 1 to 2 days, as shown in Figure 4b. The four sets of samples showed generally increasing trends and increasing rates of chemical shrinkage in the first 8 h, while MKG-SCA showed slightly lower chemical shrinkage at the end of 8 h than the other three composites. In the following testing period, the chemical shrinkage of the MKG increased much faster than that of the organically modified geopolymer composites, with a higher increase than that of the three organically modified geopolymer composites. Compared to the MKG, the chemical shrinkage of MKG-SCA, MKG-WER, and MKG-WER-SCA on the 7th day decreased by 58.8%, 47.9%, and 46.4%, respectively. Different from drying shrinkage and chemical shrinkage, the autogenous shrinkage of the MKG showed a linear upward trend in the period from the final setting to the 18th h and then gradually stabilized, as illustrated in Figure 4c,d. MKG-SCA, MKG-WER, and MKG-WER-SCA showed negligible autogenous shrinkage in the first 9 h after the final setting and then developed with different trends. The autogenous shrinkage of MKG-WER increased from the 9th h to 18th h and then tended to be stable. The autogenous shrinkage of MKG-SCA and MKG-WER-SCA had similar trends, increasing from the 9th to the 16th hr, then decreasing to 82.19 and 43.55 μm/m at the 24th h and further to −110.32 and −296.39 μm/m at the 48th h (see Figure 4c), and finally stabilizing. This indicated that MKG-SCA and MKG-WER-SCA had slight volumetric expansion after the first 24 h. After 7 days of curing, all organically modified geopolymers showed a decrease in autogenous shrinkage, with MKG-SCA and

MKG-WER-SCA exhibiting expansion. Compared to the MKG, the autogenous shrinkage of MKG-SCA, MKG-WER, and MKG-WER-SCA decreased by 111.4%, 64.7%, and 131.2%, respectively.
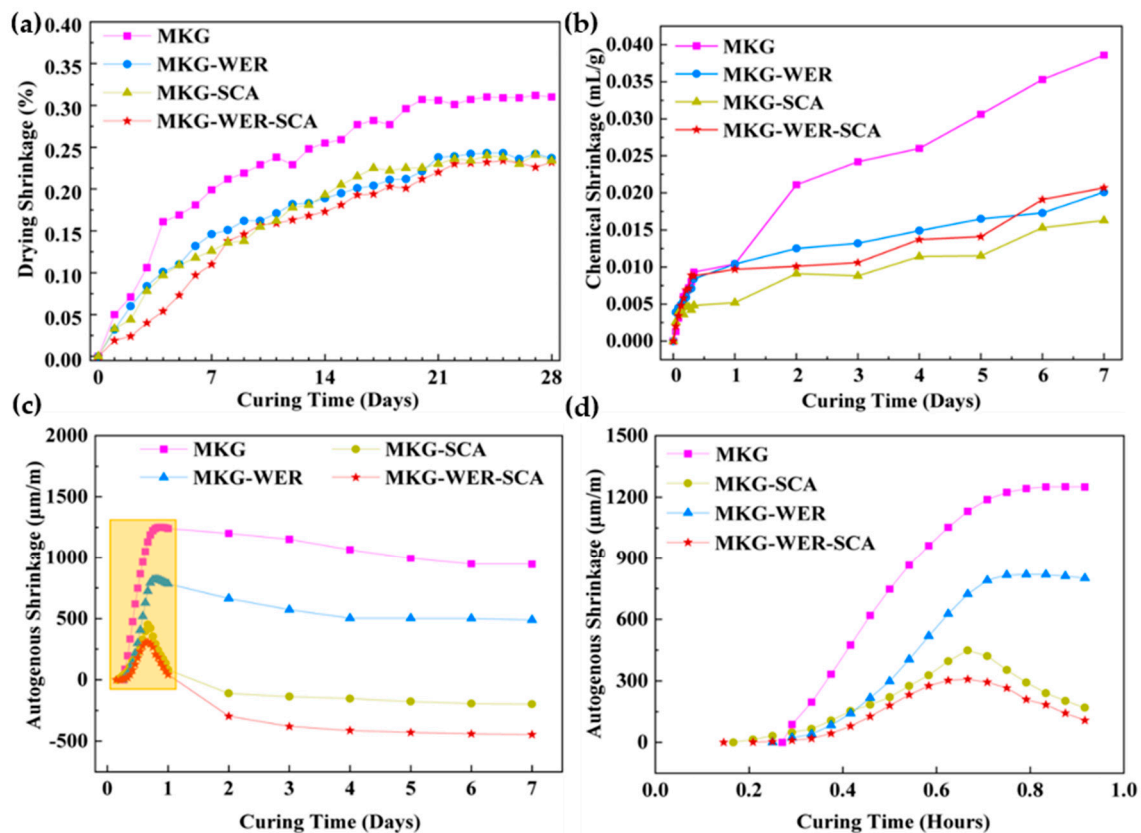

Figure 4. The (**a**) drying shrinkage, (**b**) chemical shrinkage, and (**c**) autogenous shrinkage during the curing of 7 days and (**d**) autogenous shrinkage during the curing of the first 24 h of MKG, MKG-SCA, MKG-WER, and MKG-WER-SCA composites.

Metakaolin underwent a dissolution–polymerization–polycondensation process with alkali activation [50]. First, metakaolin was rapidly dissolved in the alkaline aqueous solution, generating a large number of silicate and aluminate oligomers [42]. During this process, the density of the material decreased, and the chemical shrinkage of the MKG had a monotonically increasing period. Since autogenous shrinkage includes both chemical shrinkage and self-desiccation, the autogenous shrinkage of the MKG showed the same trend. Afterward, the aluminate oligomers further polymerized with the silicate oligomers in the pore water and formed a silica-rich amorphous geopolymer network [51]. MK underwent drastic self-desiccation and gradually hardened, and the autogenous shrinkage of the MKG further developed. However, part of the WER and SCA in the organically modified geopolymer composites covered the surface of the metakaolin to form a coating film and hinder the reaction process [52,53]. As a result, MKG-SCA, MKG-WER, and MKG-WER-SCA had lower chemical shrinkage and slower autogenous shrinking rates than the MKG in the early stage.

On the other hand, the WER and SCA reacted with the geopolymer gel to form a more ductile micro-network and fix more water molecules [54,55]. Some of the WER in the form of spheres and films can also partially fill or simply seal the capillary pores, contributing to a denser porous structure [56]. The SCA has the structure of R_n-S-$X_{(4-n)}$ ($n = 1, 2$), where X stands for alkoxy, and R stands for an organo-functional group, enabling it to react with the geopolymer gel and the WER simultaneously [57,58]. The SCA acted as a bridge between the organic agent and the inorganic substances, resulting in a more compact three-

dimensional network structure of the MKG composites. At the same time, water molecules were more stably retained in the networks of MKG composites. This would significantly reduce the drying shrinkage, which is induced by the evaporation of unbound or free water from the geopolymer matrix [59]. As a result, MKG-SCA, MKG-WER, and MKG-WER-SCA had lower drying shrinkage than the MKG. At the same time, the incorporation of the WER and SCA produced more a-Anatase, b-Phlogopite-1M, and c-Calcite in the geopolymer, leading to a slight expansion and a decrease in the autogenous shrinkage of the geopolymer, as shown in Figure 4c. These will be further discussed in Section 3.2.

It was revealed that the incorporation of 1 wt% SCA and 20 wt% WER reduced the drying shrinkage of the MKG significantly, particularly the combination of the SCA and WER. As the chemical shrinkage and the autogenous shrinkage of the MKG composites were decreased, the drying shrinkage is suggested to have been reduced by the modification of the microstructure of the geopolymerization products by the organic liquids.

3.2. Microstructure and Modification Mechanism

3.2.1. Micromorphology and Porosity

The effects of the WER and SCA on the microstructure of the MKG were investigated by characterizing the micromorphology and porosity of the SCA- and WER-modified MKG. As shown in Figure 5a, relatively wide and long microcracks were found in the MKG. Compared with the MKG, the microstructures of MKG-SCA, MKG-WER, and MKG-WER-SCA were denser, and the microcracks were fewer and narrower, indicating that the addition of organic modifiers increased the microstructural compactness of the MKG and reduced the generation of microcracks. The denser microstructure means less pore water and a more closed pore structure, which will reduce the consumption of pore water in the process of geopolymer dissolution and reduce the capillary stress generated by the evaporation of pore water into the external environment, thus improving the resistance to autogenous shrinkage and drying shrinkage. In addition, the resin in MKG-WER and MKG-WER-SCA was embedded in the matrix with a close connection to the surrounding geopolymer gel. As shown in the enlarged portion inserted in Figure 5c,d, the surface of the resin spheres in MKG-WER was smooth, while that in MKG-WER-SCA had many "pits", which might be caused by the chemical reaction between the SCA and WER.

As shown in Figure 6, the interface between the WER and the geopolymer matrix was characterized by SEM-EDS. The content of carbon (C) greatly changed along the scanning line, which gradually changed from a matrix to a resin and from a resin to a matrix (see Figure 6b). This indicates great compatibility between the resin and the geopolymer gel. Sodium (Na) and aluminum (Al) showed an overall stable trend along the scan line, while oxygen (O) was higher in the resin region than in the matrix region, and silicon (Si) was lower in the matrix region. This indicates that Al and Na are evenly distributed across the resin and the matrix, with more O in the resin region and more Si in the matrix region. In addition, a point of interest on the resin and geopolymer matrix was selected and characterized by EDS, the spectrum of which is illustrated in Figure 6c,d, respectively. The main elements of Point 1 (on the resin) and Point 2 (on the geopolymer) both contain the elements C, Si, Al, Na, and O. For the WER (Point 1), C and O were the main elements in the resin, and the high content of Si could come from the SCA and the adhered geopolymer and Al from the adhered geopolymer. On the other hand, the C and Si in the spectrum of Point 2 (on the geopolymer) could partially originate from the SCA and WER linked in the geopolymer matrix. In this case, the SCA acted as a bridge between the WER and MKG, reacting with both the resin and the aluminosilicate products and strengthening the connection between these two materials [57].

To verify the densification effect of the organic–inorganic interaction on the microstructure of the MKG composites, the porosity of the MKG, MKG-WER, MKG-SCA, and MKG-WER-SCA was characterized by MIP. The pore size distribution of the composites after curing for 28 days and a diagram of the pore volume in different size ranges are shown in Figure 7. The pores of the four samples were mainly in the micropore (<100 nm) range. The

proportions of mesopores (100 nm–1000 nm) and macropores (>1000 nm) were relatively small. The volume of the micropores of MKG-WER, MKG-SCA and MKG-WER-SCA was higher than that of the MKG, while the mesopore and macropore volume showed the opposite trend. Compared to the MKG, the total volume of mesopores and macropores in MKG-WER, MKG-SCA, and MKG-WER-SCA decreased by 11.5%, 8.7%, and 3.8%, respectively. The total pore volume of the SCA- and WER-modified geopolymer composites was higher than that of the MKG, with MKG-WER-SCA having the highest pore volume due to the significantly increased volume of micropores and the higher pore size of the dominant micropore, as shown in Figure 7a,b. The chain-like organic resin molecules of MKG-WER-SCA and MKG-WER filled the voids and converted macropores into micropores, resulting in a more compact microstructure, although the total pore volume increased. In addition, "small pits" formed on the surface of MKG-WER-SCA (see Figure 5d), which can be another reason for the large increase in micropores in MKG-WER-SCA. The main diameters of the micropores in MKG-WER-SCA and MKG-WER were larger than those of the MKG and MKG-SCA (see Figure 7a). The film formed by the WER blocked a portion of the hollow pore channels, creating closed pores and affecting the migration of water. However, under the high pressure of the mercury intrusion test, the film would break, and the presence of these pores still remained detectable, increasing the porosity and pore diameter of MKG-WER-SCA and MKG-WER [60].
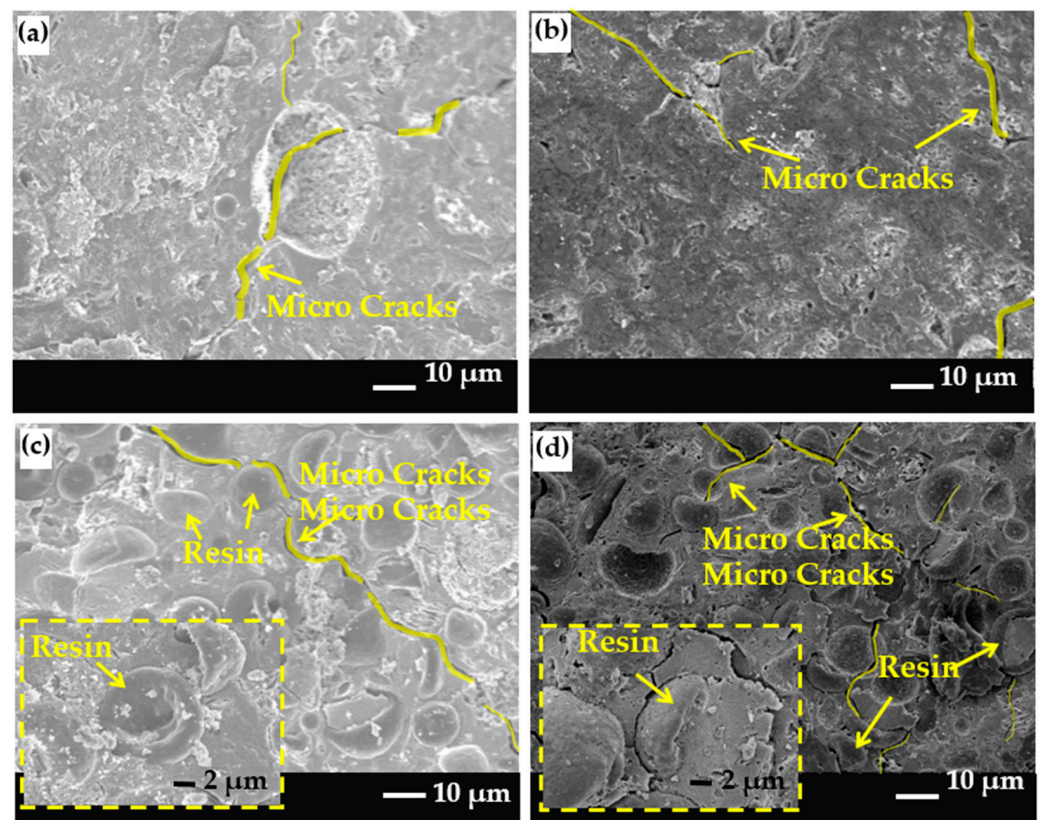

Figure 5. The SEM images of (**a**) MKG, (**b**) MKG-SCA, (**c**) MKG-WER, and (**d**) MKG-WER-SCA cured for 28 days.
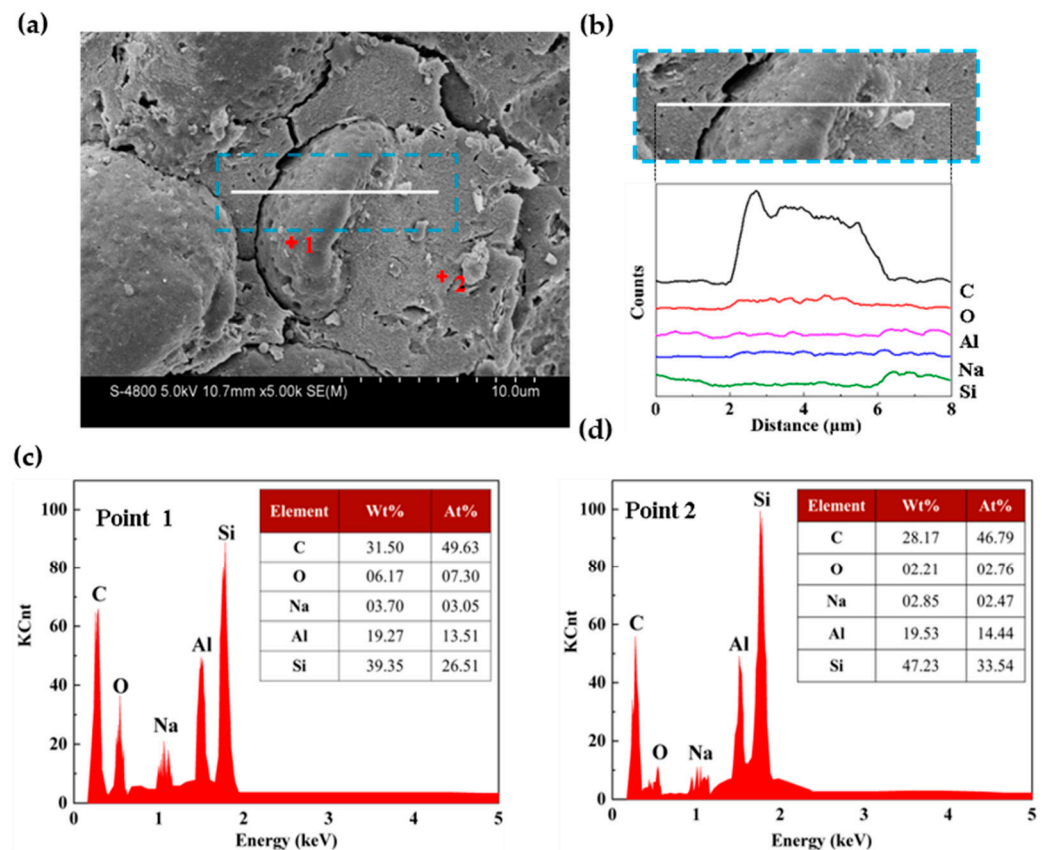
Figure 6. (**a**) The SEM image of MKG−WER−SCA and the EDS spectra of (**b**) the line scanned across the WER and geopolymer matrix, (**c**) Point 1, and (**d**) Point 2 in (**a**).
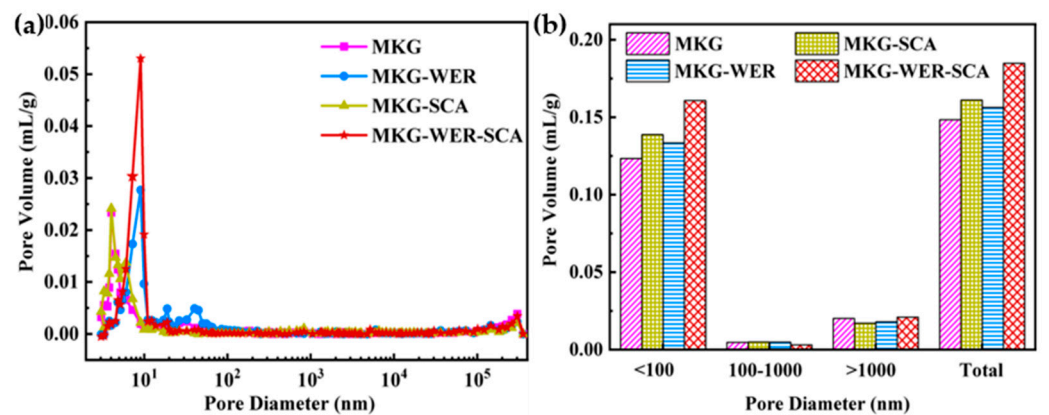

Figure 7. The (**a**) pore size distribution volume and (**b**) the volume of the pores in different size ranges of composites.

3.2.2. Characteristic Bonds and Mineralogy

As shown in Figure 8a, the characteristic bonds of the MKG, MKG-SCA, MKG-WER, and MKG-WER-SCA composite pastes were characterized by FTIR. The bands at 3450~3570 cm^{-1} and 1650 cm^{-1} in the patterns of all four samples were attributed to O-H stretching vibrations and bending vibrations, respectively [28]. The peak centered at 1040 cm^{-1} was attributed to the stretching vibration of Si-O-X (X represents Al or Si) [61], and the band at 703 cm^{-1} was attributed to the symmetric stretching vibration of Si-O-X [28,62], indicating the polymerization of Si-O oligomers and the formation of geopolymer gels. Moreover, the intensities of these two peaks in MKG-SCA, MKG-WER, and MKG-WER-SCA were higher than their counterparts in the MKG, indicating that the addition of

organic modifiers promotes the formation of geopolymer gels. In particular, the spectra of MKG-WER and MKG-WER-SCA were similar, and a peak at 1240 cm^{-1} with low intensity was found, which was caused by the stretching vibration of aromatic hydrocarbons in the main chain of the epoxy resin [63]. A small peak was also found at 1515 cm^{-1}, which was caused by N–H bending vibrations [26].
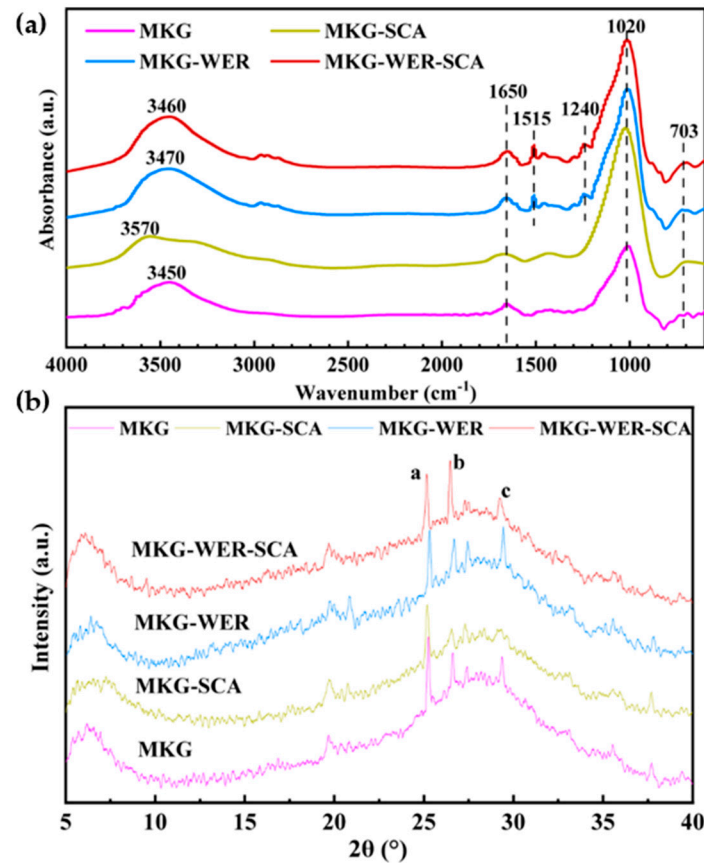

Figure 8. The (**a**) FTIR spectra and (**b**) XRD patterns of the MKG, MKG-SCA, MKG-WER, and MKG-WER-SCA after 28 days of curing (a: Anatase; b: Phlogopite-1M; c: Calcite).

As shown in Figure 8b, the mineral composition of the MKG, MKG-SCA, MKG-WER, and MKG-WER-SCA cured for 28 days was characterized by XRD. A hump in the range of 20~35° 2θ was found in the patterns of all MKG and MKG composites, indicating the formation of geopolymer gels. The strength and width of this hump of MKG-SCA were approximated to those of the MKG, indicating that the addition of the SCA in the small amount used (1wt%) had little influence on the mineralogy of the MKG. In addition, the mineral crystalline phases, including anatase (a-Anatase), phlogopite (b-Phlogopite-1M), and calcite (c-Calcite), were found in the four composites.

3.2.3. Molecular Structure

As shown in Figure 9a, the ^{27}Al MAS NMR spectra of the MKG, MKG-SCA, MKG-WER, and MKG-WER-SCA all had only one peak at 57.5 ppm, which was the typical signal of IV-coordinated Al, indicating that the Al polymerization of [Al(OH)$_4$]$^-$ in the MKG and the MKG composites was complete [64]. This was mainly due to the faster and higher reaction rate of polymerization between aluminate and silicate than polymerization between silicates. During the reaction, [Al(OH)$_4$]$^-$ groups with a negative charge were more stable than Si due to the larger atomic size and higher local charge of the Al atom. Meanwhile, polymerization involving aluminate oligomers might occur more easily due to the four hydroxyl groups of [Al(OH)$_4$]$^-$ [51,65]. The intensity of the signal at 57.5 ppm of

MKG-WER and MKG-WER-SCA was obviously higher than that of the MKG. This might be due to the fact that the strong basicity of DETA introduced by the WER improved the alkalinity of the MKG matrix and promoted the dissolution of MK, releasing more $[Al(OH)^4]^-$, $[SiO(OH)^3]^-$, and $[SiO_2(OH)^2]^{2-}$ [51] and improving the degree of polymerization. On the other hand, the SCA increased the number of Si-O bridging bonds, which would suppress the polycondensation of Al to a certain extent, and decreased the intensity of this peak in MKG-SCA and MKG-WER-SCA compared to the MKG and MKG-WER, respectively [66]. As shown in Figure 9b, the ^{29}Si MAS NMR spectra of the MKG, MKG-SCA, MKG-WER, and MKG-WER-SCA all had a wide hump in the range of $-120 \sim -60$ ppm, indicating that a stable Si coordination sphere had formed [35]. However, the humps of MKG-SCA and MKG-WER-SCA were shifted to more negative wavenumbers compared to the MKG and MKG-WER, respectively. It might be due to the fact that the Si-O- of the SCA bonded with -Si-O-Si- and -Si-O-Al- in the MKG matrix, changing the stable Si coordination.
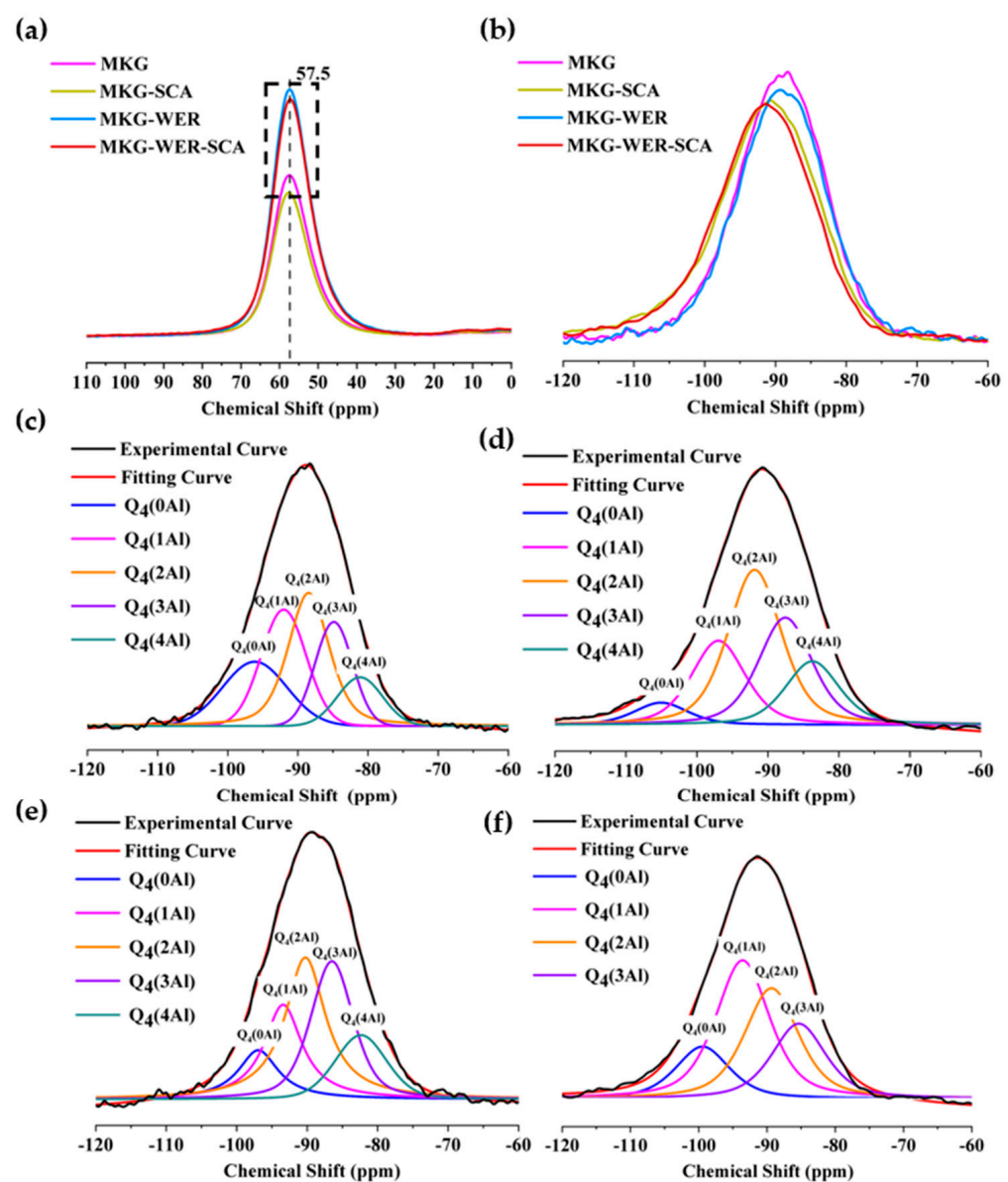

Figure 9. The (**a**) ^{27}Al and (**b**) ^{29}Si MAS NMR spectra of the MKG, MKG-SCA, MKG-WER, and MKG-WER-SCA. The deconvolution fitting of ^{29}Si MAS NMR spectrum of (**c**) the MKG, (**d**) MKG-SCA, (**e**) MKG-WER, and (**f**) MKG-WER-SCA (note: the black lines represent experimental curves; the red lines represent the fitting curves; the remaining lines represent the fitting peaks).

To investigate the coordination environment of Si more comprehensively, deconvolution analysis was performed on the 29Si MAS NMR spectra of the composites. As shown in Figure 9c–f, the peak in the 29Si MAS NMR spectrum in the range of $-70\sim-120$ ppm was deconvoluted to Q4(mAl), where Q4 is the Si tetrahedron connected to four bridging O atoms, and m is the number of aluminum atoms connected to [SiO4] units via bridging oxygen [65,67]. The fitted peaks were assigned to Q4(0Al), Q4(1Al), Q4(2Al), Q4(3Al), and Q4(4Al), indicating that a highly polymerized three-dimensional structure was formed in the MKG and all organically modified MKG composites. In addition, the proportion of each type of Q4(mAl) was calculated by dividing the area of the deconvoluted Gaussian peak by the total area of the experimental curve, as listed in Table 4 [67]. The peaks of different Q4(mAl) coordinates in MKG-SCA, MKG-WER, and MKG-WER-SCA all shifted in a more negative direction than in the MKG, indicating that the number of polymers including monomers and small oligomers of the MKG decreased after the incorporation of organic modifiers, and the degree of polymerization of organically modified MKGs increased [35]. The proportion of Q4(2Al), Q4(3Al), and Q4(4Al) in MKG-SCA and MKG-WER increased compared to the MKG, indicating that the addition of the WER and SCA promoted the formation of higher-polymerized -Si-O-Al- and -Si-O-Si-. At the same time, the fraction of Q4(1Al) in MKG-WER-SCA was higher than in MKG-WER and MKG-SCA, while Q4(2Al) and Q4(3Al) showed the opposite trend. This indicates that more -Si-O-Al- bonds tend to form in the geopolymer when the WER and SCA are used synergistically [68]. This is consistent with the XRD results, where the Phlogopite-1M peak of MKG-WER-SCA was clearly higher than those of MKG-WER and MKG-SCA (see Figure 8b).

Table 4. Signal positions and ratios of deconvoluted peaks.

Peaks	MKG		MKG-WER		MKG-SCA		MKG-WER-SCA	
	Signal Position (ppm)	Ratio (%)	Signal Position (ppm)	Ratio (%)	Signal Position (ppm)	Ratio (%)	Signal Position (ppm)	Ratio (%)
Q_4(0Al)	-96.2	18.68	-96.9	10.64	-105.1	5.12	-99.4	13.97
Q_4(1Al)	-92.0	24.04	-93.4	19.46	-97.0	19.46	-93.6	36.78
Q_4(2Al)	-88.5	29.77	-90.3	31.19	-91.9	35.89	-89.3	29.38
Q_4(3Al)	-84.9	17.57	-86.5	25.59	-87.6	24.82	-85.3	19.97
Q_4(4Al)	-81.2	9.94	-82.4	13.12	-83.7	14.70	--	--

3.2.4. Polymerization Mechanism

Based on the above results and observations, we propose a reasonable reaction process among the SCA, WER, and MKG, as illustrated in Figure 10. In the first step, the aluminosilicate mineral components in MK dissolved in the alkali solution and released $Si(OH)_4$ and $Al(OH)_4^-$. Secondly, the released $Si(OH)_4$ and $Al(OH)_4^-$ in the alkali solution polymerized and formed aluminosilicate oligomers, while the WER opened the epoxy ring of the epoxy resin to form hydroxyl groups, and the SCA hydrolyzed to form silanol groups ($\equiv$Si-OH). In the third step, the hydroxyl groups formed by the WER were hydrogen-bonded by reacting with the hydroxyl groups in the aluminosilicate oligomers and water molecules. Furthermore, the silanol groups formed by the SCA and the Si-OH and Al-OH groups in the aluminosilicate oligomers polymerized to form -Si-O-Si- and -Si-O-Al- bonds. At the same time, the alkoxy groups ($-OCH_3$ or $-OC_2H_5$) in the SCA were bound to the opened rings of the WER, resulting in a dense organic–inorganic WER-SCA-MKG network formed by the bridging SCA between the WER and MKG gel [55,69].

The dissolution of metakaolin in the first stage was the most important factor influencing the chemical shrinkage of the MKG. The chemical shrinkage of MKG-WER-SCA and MKG-WER was larger than that of MKG-SCA, which can be attributed to the strong base (i.e., DETA) introduced by the WER, which promotes the dissolution of metakaolin [51]. Later, the WER opened its ring, and the SCA was hydrolyzed to form silanol groups. At

this point, the products of the WER and SCA might attach to the aluminosilicate oligomers generated by the alkali activation of metakaolin, forming a film that prevents further polymerization [43]. This is consistent with the almost disappearance of autogenous shrinkage in MKG-WER-SCA, MKG-WER, and MKG-SCA in the early stage. Eventually, a dense organic–inorganic was formed to fix more water molecules, and MKG-WER-SCA exhibited the lowest drying shrinkage [59]. From the microstructural point of view, the intensity of MKG-WER-SCA, MKG-WER, and MKG-SCA peaks in FTIR (see Figure 8a) at 1040 cm^{-1} and 703 cm^{-1} was higher than that of the MKG. The total pore volume of MKG-WER-SCA, MKG-WER, and MKG-SCA was larger than that of the pure geopolymer (see Figure 7b). This indicates that a denser resin–gel structure was formed, which is confirmed by the SEM images of MKG-WER-SCA (see Figure 6d). These findings elucidate the formation of the organic–inorganic WER-SCA-MKG network.
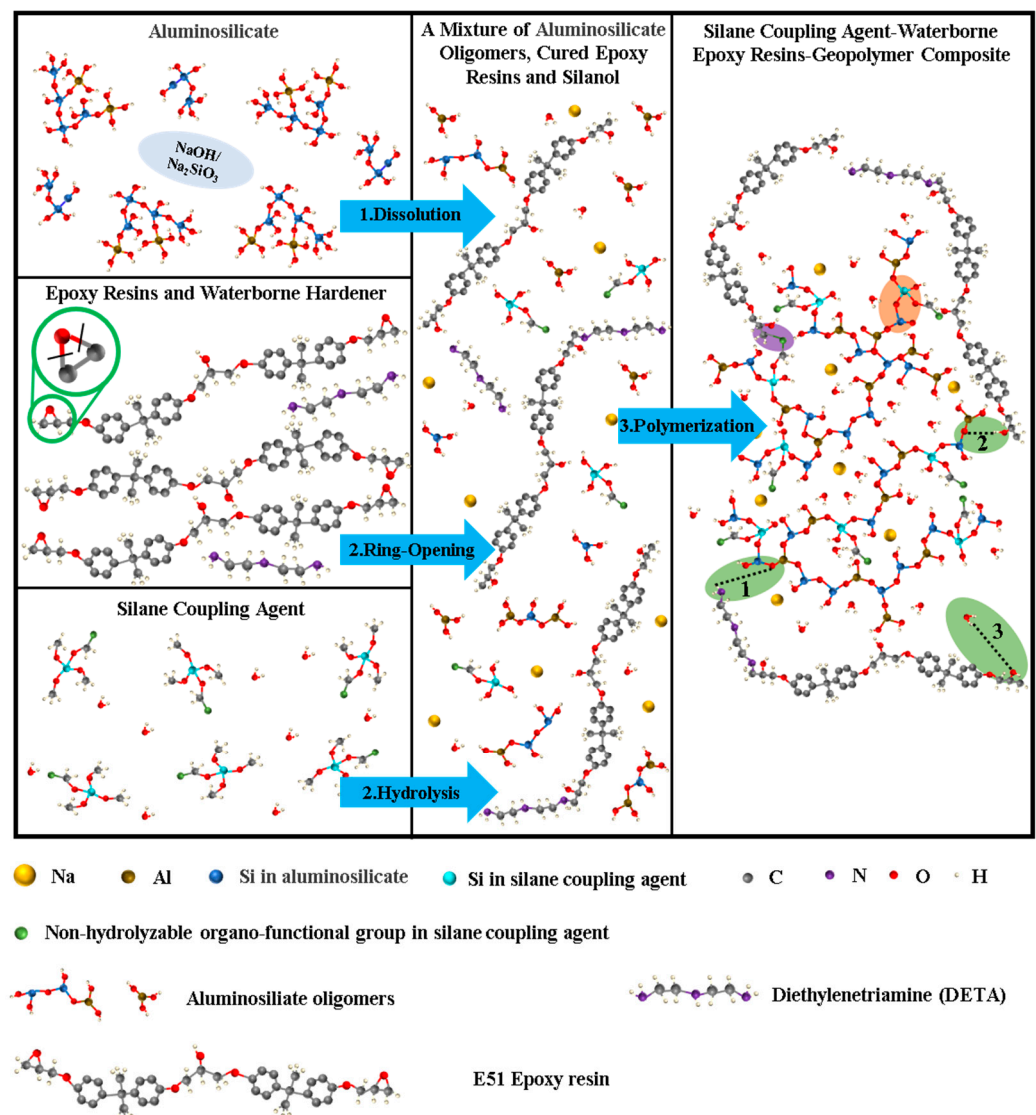

Figure 10. A conceptual model of the reaction of MKG-WER-SCA (note: dashed lines "1, 2, 3" represent the hydrogen bonds formed between the amino and hydroxyl groups in the WER and the hydroxyl and water molecules in the MKG; the purple area is the bonding of the WER to the SCA; the orange area is the SCA bonded to the MKG network).

3.3. Resistance to Chloride Ion Penetration

The shrinkage and induced cracks at different scales have a significant influence on the permeability of cementitious materials. The higher shrinkage of the MKG can lead

to surface cracks in the specimen, which are susceptible to chloride ion penetration, thus promoting the diffusion of chloride ions [70]. In this case, the chloride ion penetration of the MKG and MKG composites was assessed. The 2~3 mm thick coatings of the MKG, MKG-WER, MKG-SCA, and MKG-WER-SCA were applied to the concrete samples and tested with the RCM test to evaluate the resistance of the MKG and MKG composites to chloride ion penetration. After the RCM test, a AgNO₃ solution was sprayed on the section of the concrete samples, and the color of the Cl⁻-penetrated area turned white. The boundary of the white area was marked with a red dotted line, as shown in Figure 11. The penetration depth of Cl⁻ in the three composite-coated concrete samples was lower than that in the uncoated concrete and MKG-coated concrete specimens. As shown in Figure 12, the diffusion coefficient of Cl⁻ (D_{RCM}) of each sample was calculated according to the diffusion depth. The D_{RCM} of the MKG-coated concrete was 2.6×10^{-12} m²/s, 29.7% lower than that of the uncoated concrete, which was 3.7×10^{-12} m²/s. The D_{RCM} of the three MKG composite-coated concrete samples varied in the range of 1.5×10^{-12} to 1.8×10^{-12} m²/s, which was 51.4% to 59.5% lower than that of the control group and 30.8% to 42.3% lower than that of the MKG-coated sample. This showed that the protective coatings of the MKG and MKG composites effectively inhibited the diffusion of Cl⁻, with MKG-SCA having the best apparent protective effect. On the other hand, the D_{RCM} values of the control group and MKG-coated concrete were between 2×10^{-12} and 8×10^{-12} m²/s, which showed that the concrete had good resistance to the penetration of Cl⁻ according to the standard (see Table 5) proposed by Tang [71]. The chloride ion diffusion coefficients of MKG-WER-, MKG-SCA-, and MKG-WER-SCA-coated concrete were all less than 2×10^{-12} m²/s, indicating that the WER and SCA-modified MKG had better resistance to Cl⁻ penetration, verifying their lower shrinkage and denser microstructure.
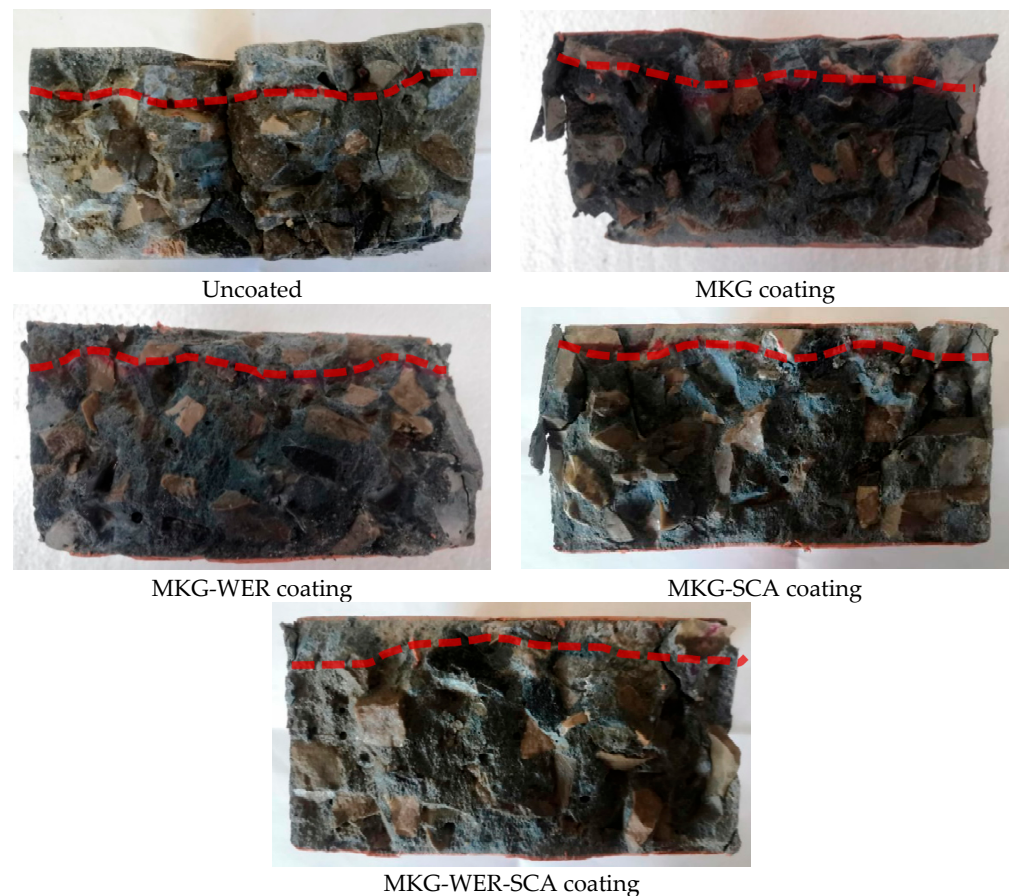

<div align="center">Uncoated MKG coating</div>

<div align="center">MKG-WER coating MKG-SCA coating</div>

<div align="center">MKG-WER-SCA coating</div>

Figure 11. The cross-sections of all samples tested with the RCM method (note: the white area above the red dashed line is the Cl⁻ penetration depth).
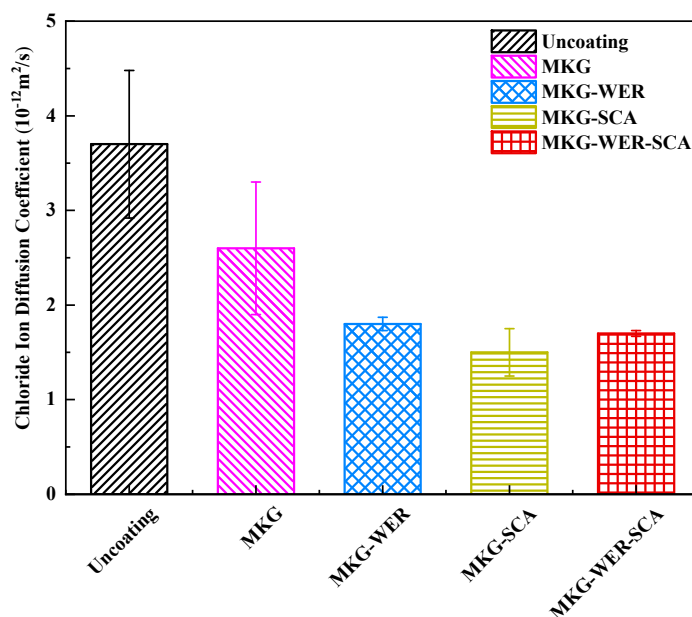
Figure 12. Chloride ion diffusion coefficients of concrete with and without MKG composite coatings.

Table 5. Reference standard for chloride ion diffusion coefficient [71].

Apparent Diffusion Coefficient of Chloride ions ($D_a/10^{-12}$ m^2/s)	Concrete Properties
<2	Very good resistance to chloride ion penetration
<8	Good resistance to chloride ion penetration
<16	General resistance to chloride ion penetration
>16	Not suitable for harsh environments

4. Conclusions

The shrinkage properties of the MKG were modified with a WER, an SCA, and a synergistic modifier consisting of the WER and SCA. The chemical shrinkage, autogenous shrinkage, and drying shrinkage of the organic-agent-modified MKG were tested, and the modification mechanisms were investigated. Finally, the improved volumetric stability of MKG composites was verified by assessing the resistance of chloride ion penetration of the MKG composite coatings. Accordingly, the following conclusions can be drawn:

1. The addition of the SCA, WER, and mixture of these two agents significantly reduced the drying shrinkage, chemical shrinkage, and autogenous shrinkage of the MKG. The chemical shrinkage and shrinkage rate of the SCA-modified MKG were the lowest, while the synergistic modification by the WER and SCA led to the highest reduction in the autogenous shrinkage and drying shrinkage of the MKG. In particular, the MKG modified by the SCA and SCA-WER showed slight micro-expansion, which might be due to modified porosity caused by the SCA and newly formed products that increased the volume of the composites.

2. MKG-WER-SCA had the most promising performance in reducing drying shrinkage, chemical shrinkage, and autogenous shrinkage, which is mainly attributed to the densified microstructure and the "restriction" effect of the organic modifiers. The microstructure of MKG-WER-SCA was densified by the compact organic–inorganic network formed by the bridging SCA between MKG and the WER. The denser microstructure reduced the consumption of pore water during the dissolution of the geopolymer and the evaporation of pore water into the external environment, thereby reducing the drying shrinkage, chemical shrinkage, and autogenous shrinkage. Furthermore, the coating film of WER-SCA restricted the chemical shrinkage and autogenous shrinkage of the MKG.

3. The improved chloride permeability of concrete with the organically modified MKG coating further confirmed the improved shrinkage resistance of MKG-WER, MKG-SCA, and MKG-WER-SCA. The chloride ion diffusion coefficient of organically modified geopolymer-coated concrete was 2×10^{-12} m^2/s and 51.4~59.5% lower than that without a coating compared with the control group. This indicates that MKG composite coatings can effectively inhibit the diffusion of chloride ions and be applied in concrete protective coatings for marine engineering.

Author Contributions: M.Z.: conceptualization, writing—review and editing. Y.Z.: Data curation, investigation, writing—original draft. L.S.: methodology, resources, writing—review and editing. All authors have read and agreed to the published version of the manuscript.

Data Availability Statement: The raw data supporting the conclusions of this article will be made available by the authors on request.

Conflicts of Interest: The authors declare that they have no known competing financial interests or personal relationships that could have appeared to influence the work reported in this paper.

References

1. Kim, B.; Lee, S. Review on characteristics of metakaolin-based geopolymer and fast setting. *J. Korean Ceram. Soc.* **2020**, *57*, 368–377. [CrossRef]
2. Patil, S.; Karikatti, V.; Chitawadagi, M. Granulated Blast-Furnace Slag (GGBS) based Geopolymer Concrete–Review. *Int. J. Adv. Sci. Eng* **2018**, *5*, 879–885. [CrossRef]
3. Abdel-Ghani, N.T.; Elsayed, H.A.; AbdelMoied, S. Geopolymer synthesis by the alkali-activation of blastfurnace steel slag and its fire-resistance. *Hbrc J.* **2018**, *14*, 159–164. [CrossRef]
4. Yang, H.; Liu, L.; Yang, W.; Liu, H.; Ahmad, W.; Ahmad, A.; Aslam, F.; Joyklad, P. A comprehensive overview of geopolymer composites: A bibliometric analysis and literature review. *Case Stud. Constr. Mater.* **2022**, *16*, e00830. [CrossRef]
5. Guo, X.; Yang, J. Intrinsic properties and micro-crack characteristics of ultra-high toughness fly ash/steel slag based geopolymer. *Constr. Build. Mater.* **2020**, *230*, 116965. [CrossRef]
6. Nair, B.; Zhao, Q.; Cooper, R. Geopolymer matrices with improved hydrothermal corrosion resistance for high-temperature applications. *J. Mater. Sci.* **2007**, *42*, 3083–3091. [CrossRef]
7. Tong, L.; Zhao, J.; Cheng, Z. Chloride ion binding effect and corrosion resistance of geopolymer materials prepared with seawater and coral sand. *Constr. Build. Mater.* **2021**, *309*, 125126. [CrossRef]
8. Najafi, E.K.; Chenari, R.J.; Arabani, M. The potential use of clay-fly ash geopolymer in the design of active-passive liners: A review. *Clays Clay Miner.* **2020**, *68*, 296–308. [CrossRef]
9. Jiang, C.; Wang, A.; Bao, X.; Ni, T.; Ling, J. A review on geopolymer in potential coating application: Materials, preparation and basic properties. *J. Build. Eng.* **2020**, *32*, 101734. [CrossRef]
10. Jindal, B.B.; Alomayri, T.; Hasan, A.; Kaze, C.R. Geopolymer concrete with metakaolin for sustainability: A comprehensive review on raw material's properties, synthesis, performance, and potential application. *Environ. Sci. Pollut. Res.* **2023**, *30*, 25299–25324. [CrossRef]
11. Duan, P.; Yan, C.; Luo, W. A novel waterproof, fast setting and high early strength repair material derived from metakaolin geopolymer. *Constr. Build. Mater.* **2016**, *124*, 69–73. [CrossRef]
12. Zarina, Y.; Al Bakri Abdullah, M.M.; Kamarudin, H.; Nizar, I.K.; Razak, R.A. Reviews on the geopolymer materials for coating application. *Adv. Mater. Res.* **2013**, *626*, 958–962. [CrossRef]
13. Zhang, Z.; Yao, X.; Wang, H. Potential application of geopolymers as protection coatings for marine concrete III. Field experiment. *Appl. Clay Sci.* **2012**, *67*, 57–60. [CrossRef]
14. Li, N.; Zhang, Z.; Shi, C.; Zhang, J. Some progresses in the challenges for geopolymer. *IOP Conf. Ser. Mater. Sci. Eng.* **2018**, *431*, 022003. [CrossRef]
15. Vilaplana, J.L.; Baeza, F.J.; Galao, O.; Alcocel, E.; Zornoza, E.; Garcés, P. Mechanical properties of alkali activated blast furnace slag pastes reinforced with carbon fibers. *Constr. Build. Mater.* **2016**, *116*, 63–71. [CrossRef]
16. Ma, H.; Zhu, H.; Chen, H.; Ni, Y.; Xu, X.; Huo, Q. Shrinkage-reducing measures and mechanisms analysis for alkali-activated coal gangue-slag mortar at room temperature. *Constr. Build. Mater.* **2020**, *252*, 119001. [CrossRef]
17. Al-Mashhadani, M.M.; Canpolat, O.; Aygörmez, Y.; Uysal, M.; Erdem, S. Mechanical and microstructural characterization of fiber reinforced fly ash based geopolymer composites. *Constr. Build. Mater.* **2018**, *167*, 505–513. [CrossRef]
18. Junior, J.; Saha, A.K.; Sarker, P.K.; Pramanik, A. Workability and Flexural Properties of Fibre-Reinforced Geopolymer Using Different Mono and Hybrid Fibres. *Materials* **2021**, *14*, 4447. [CrossRef]

19. Farhan, N.A.; Sheikh, M.N.; Hadi, M.N. Engineering Properties of Ambient Cured Alkali-Activated Fly Ash–Slag Concrete Reinforced with Different Types of Steel Fiber. *Am. Soc. Civ. Eng.* **2018**, *30*, 04018142. [CrossRef]

20. Rashad, A.M. Effect of steel fibers on geopolymer properties–the best synopsis for civil engineer. *Constr. Build. Mater.* **2020**, *246*, 118534. [CrossRef]

21. Samal, S.; Blanco, I. An Application Review of Fiber-Reinforced Geopolymer Composite. *Fibers* **2021**, *9*, 23. [CrossRef]

22. Colangelo, F.; Roviello, G.; Ricciotti, L.; Ferone, C.; Cioffi, R. Preparation and characterization of new geopolymer-epoxy resin hybrid mortars. *Materials* **2013**, *6*, 2989–3006. [CrossRef]

23. Wang, X.; Zhang, C.; Wu, Q.; Zhu, H.; Liu, Y. Thermal properties of metakaolin-based geopolymer modified by the silane coupling agent. *Mater. Chem. Phys.* **2021**, *267*, 124655. [CrossRef]

24. Zhang, C.; Wang, X.; Hu, Z.; Wu, Q.; Zhu, H.; Lu, J. Long-term performance of silane coupling agent/metakaolin based geopolymer. *J. Build. Eng.* **2021**, *36*, 102091. [CrossRef]

25. Liang, G.; Zhu, H.; Zhang, Z.; Wu, Q. Effect of rice husk ash addition on the compressive strength and thermal stability of metakaolin based geopolymer. *Constr. Build. Mater.* **2019**, *222*, 872–881. [CrossRef]

26. Ferone, C.; Roviello, G.; Colangelo, F.; Cioffi, R.; Tarallo, O. Novel hybrid organic-geopolymer materials. *Appl. Clay Sci.* **2013**, *73*, 42–50. [CrossRef]

27. Roviello, G.; Ricciotti, L.; Tarallo, O.; Ferone, C.; Colangelo, F.; Roviello, V.; Cioffi, R. Innovative fly ash geopolymer-epoxy composites: Preparation, microstructure and mechanical properties. *Materials* **2016**, *9*, 461. [CrossRef]

28. Roviello, G.; Ricciotti, L.; Ferone, C.; Colangelo, F.; Cioffi, R.; Tarallo, O. Synthesis and characterization of novel epoxy geopolymer hybrid composites. *Materials* **2013**, *6*, 3943–3962. [CrossRef]

29. Saludung, A.; Ogawa, Y.; Kawai, K. Microstructure and mechanical properties of epoxy resin-reinforced geopolymer exposed to high temperatures. *Mater. Lett.* **2023**, *331*, 133473. [CrossRef]

30. Du, J.; Bu, Y.; Shen, Z.; Hou, X.; Huang, C. Effects of epoxy resin on the mechanical performance and thickening properties of geopolymer cured at low temperature. *Mater. Des.* **2016**, *109*, 133–145. [CrossRef]

31. Ma, Y.; Ye, G. The shrinkage of alkali activated fly ash. *Cem. Concr. Res.* **2015**, *68*, 75–82. [CrossRef]

32. Neto, A.A.M.; Cincotto, M.A.; Repette, W. Drying and autogenous shrinkage of pastes and mortars with activated slag cement. *Cem. Concr. Res.* **2008**, *38*, 565–574. [CrossRef]

33. Lee, N.; Jang, J.G.; Lee, H.-K. Shrinkage characteristics of alkali-activated fly ash/slag paste and mortar at early ages. *Cem. Concr. Compos.* **2014**, *53*, 239–248. [CrossRef]

34. Mastali, M.; Kinnunen, P.; Dalvand, A.; Firouz, R.M.; Illikainen, M. Drying shrinkage in alkali-activated binders—A critical review. *Constr. Build. Mater.* **2018**, *190*, 533–550. [CrossRef]

35. Li, Z.; Zhang, S.; Zuo, Y.; Chen, W.; Ye, G. Chemical deformation of metakaolin based geopolymer. *Cem. Concr. Res.* **2019**, *120*, 108–118. [CrossRef]

36. Khatib, J.M.; Ramadan, R.; Ghanem, H.; Elkordi, A.; Sonebi, M. Effect of limestone fines as a partial replacement of cement on the chemical, autogenous, drying shrinkage and expansion of mortars. *Mater. Today Proc.* **2022**, *58*, 1199–1204. [CrossRef]

37. Thomas, R.; Lezama, D.; Peethamparan, S. On drying shrinkage in alkali-activated concrete: Improving dimensional stability by aging or heat-curing. *Cem. Concr. Res.* **2017**, *91*, 13–23. [CrossRef]

38. Luo, L.; Yao, W.; Liang, G.; Luo, Y. Workability, autogenous shrinkage and microstructure of alkali-activated slag/fly ash slurries: Effect of precursor composition and sodium silicate modulus. *J. Build. Eng.* **2023**, *73*, 106712. [CrossRef]

39. Kumarappa, D.B.; Peethamparan, S.; Ngami, M. Autogenous shrinkage of alkali activated slag mortars: Basic mechanisms and mitigation methods. *Cem. Concr. Res.* **2018**, *109*, 1–9. [CrossRef]

40. Li, Z.; Liang, X.; Chen, Y.; Ye, G. Effect of metakaolin on the autogenous shrinkage of alkali-activated slag-fly ash paste. *Constr. Build. Mater.* **2021**, *278*, 122397. [CrossRef]

41. Yang, T.; Zhu, H.; Zhang, Z. Influence of fly ash on the pore structure and shrinkage characteristics of metakaolin-based geopolymer pastes and mortars. *Constr. Build. Mater.* **2017**, *153*, 284–293. [CrossRef]

42. Ruan, S.; Chen, S.; Liu, Y.; Zhang, Y.; Yan, D.; Zhang, M. Early-age deformation of hydrophobized metakaolin-based geopolymers. *Cem. Concr. Res.* **2023**, *169*, 107168. [CrossRef]

43. Tian, Z.; Liu, X.; Zhang, Z.; Zhang, K.; Tang, X. Potential using of water-soluble polymer latex modified greener road geopolymeric grouts: Its preparation, characterization and mechanism. *Constr. Build. Mater.* **2021**, *273*, 121757. [CrossRef]

44. Reeb, C.; Pierlot, C.; Davy, C.; Lambertin, D. Incorporation of organic liquids into geopolymer materials-A review of processing, properties and applications. *Ceram. Int.* **2021**, *47*, 7369–7385. [CrossRef]

45. Zhang, M.; Xu, H.; Zeze, A.L.P.; Zhang, J. Metakaolin-based geopolymer composites modified by epoxy resin and silane: Mechanical properties and organic-inorganic interaction mechanism. *Appl. Clay Sci.* **2023**, *232*, 106767. [CrossRef]

46. Zhang, M.; Xu, H.; Zeze, A.L.P.; Liu, X.; Tao, M. Coating performance, durability and anti-corrosion mechanism of organic modified geopolymer composite for marine concrete protection. *Cem. Concr. Compos.* **2022**, *129*, 104495. [CrossRef]

47. *GB/T 50082-2009*; Standard for Test Methods of Long-Term Performance and Durability of Ordinary Concrete. China Building Industry Press: Beijing, China, 2009.

48. *US-ASTM 1608-17*; Standard Test Method for Chemical Shrinkage of Hydraulic Cement Paste. ASTM International: West Conshohocken, PA, USA, 2017.

49. *US-ASTM 1698-09*; Standard Test Method for Autogenous Strain of Cement Paste and Mortar. ASTM International: West Conshohocken, PA, USA, 2009.

50. Jaya, N.A.; Yun-Ming, L.; Cheng-Yong, H.; Abdullah, M.M.A.B.; Hussin, K. Correlation between pore structure, compressive strength and thermal conductivity of porous metakaolin geopolymer. *Constr. Build. Mater.* **2020**, *247*, 118641. [CrossRef]

51. Weng, L.; Sagoe-Crentsil, K. Dissolution processes, hydrolysis and condensation reactions during geopolymer synthesis: Part I—Low Si/Al ratio systems. *J. Mater. Sci.* **2007**, *42*, 2997–3006. [CrossRef]

52. Zhang, Z.; Yan, P. Hydration kinetics of the epoxy resin-modified cement at different temperatures. *Constr. Build. Mater.* **2017**, *150*, 287–294. [CrossRef]

53. Feng, H.; Le, H.; Wang, S.; Zhang, M.H. Effects of silanes and silane derivatives on cement hydration and mechanical properties of mortars. *Constr. Build. Mater.* **2016**, *129*, 48–60. [CrossRef]

54. Yao, J.Z.; Wang, Y.C.; Xu, D.L.; Sheng, L. Mechanical performance and hydration mechanism of geopolymer composite reinforced by resin. *Mater. Sci. Eng. A* **2010**, *527*, 6574–6580.

55. Zhang, C.; Hu, Z.; Zhu, H.; Wang, X.; Gao, J. Effects of silane on reaction process and microstructure of metakaolin-based geopolymer composites. *J. Build. Eng.* **2020**, *32*, 101695. [CrossRef]

56. Guo, S.-Y.; Zhang, X.; Chen, J.-Z.; Mou, B.; Shang, H.-S.; Wang, P.; Zhang, L.; Ren, J. Mechanical and interface bonding properties of epoxy resin reinforced Portland cement repairing mortar. *Constr. Build. Mater.* **2020**, *264*, 120715. [CrossRef]

57. Tesoro, G.; Wu, Y. Silane coupling agents: The role of the organofunctional group. *J. Adhes. Sci. Technol.* **1991**, *5*, 771–784. [CrossRef]

58. Xie, Y.; Hill, C.A.; Xiao, Z.; Militz, H.; Mai, C. Silane coupling agents used for natural fiber/polymer composites: A review. *Compos. Part A Appl. Sci. Manuf.* **2010**, *41*, 806–819. [CrossRef]

59. Qomi, M.J.A.; Brochard, L.; Honorio, T.; Maruyama, I.; Vandamme, M. Advances in atomistic modeling and understanding of drying shrinkage in cementitious materials. *Cem. Concr. Res.* **2021**, *148*, 106536. [CrossRef]

60. Zhang, Z.; Zhang, H.; Liu, T.; Lv, W. Study on the micro-mechanism and structure of unsaturated polyester resin modified concrete for bridge deck pavement. *Constr. Build. Mater.* **2021**, *289*, 123174. [CrossRef]

61. Mo, Z.; Zhao, M.; Zhang, G.; Sietins, J.M.; Sergio, G.F.; Pepi, M.S.; Yan, X.; Tao, M. Reaction kinetics of red mud-fly ash based geopolymers: Effects of curing temperature on chemical bonding, porosity, and mechanical strength. *Cem. Concr. Compos.* **2018**, *93*, 175–185.

62. Zaharaki, D.; Komnitsas, K.; Perdikatsis, V. Use of analytical techniques for identification of inorganic polymer gel composition. *J. Mater. Sci.* **2010**, *45*, 2715–2724. [CrossRef]

63. Zhang, J.; Zhang, W.; Lu, J.; Zhu, C.; Lin, W.; Feng, J. Aqueous epoxy-based superhydrophobic coatings: Fabrication and stability in water. *Prog. Org. Coat.* **2018**, *121*, 201–208. [CrossRef]

64. Wang, L.Q.; Mattigod, S.V.; Parker, K.E.; Hobbs, D.T.; Mccready, D.E. Nuclear magnetic resonance studies of aluminosilicate gels prepared in high-alkaline and salt-concentrated solutions. *J. Non-Cryst. Solids* **2005**, *351*, 3435–3442. [CrossRef]

65. Sagoe-Crentsil, K.; Weng, L. Dissolution processes, hydrolysis and condensation reactions during geopolymer synthesis: Part II. High Si/Al ratio systems. *J. Mater. Sci.* **2007**, *42*, 3007–3014. [CrossRef]

66. Brochier Salon, M.C.; Belgacem, M.N. Hydrolysis-Condensation Kinetics of Different Silane Coupling Agents. *Phosphorus* **2011**, *186*, 240–254. [CrossRef]

67. Zhu, X.; Yan, D.; Fang, H.; Chen, S.; Ye, H. Early-stage geopolymerization revealed by [27]Al and [29]Si nuclear magnetic resonance spectroscopy based on vacuum dehydration. *Constr. Build. Mater.* **2021**, *266*, 121114. [CrossRef]

68. Wan, Q.; Rao, F.; Song, S.; Cholico-González, D.F.; Ortiz, N.L. Combination formation in the reinforcement of metakaolin geopolymers with quartz sand. *Cem. Concr. Compos.* **2017**, *80*, 115–122. [CrossRef]

69. Djouani, F.; Chehimi, M.M.; Benzarti, K. Interactions of fully formulated epoxy with model cement hydrates. *J. Adhes. Sci. Technol.* **2013**, *27*, 469–489. [CrossRef]

70. Dellinghausen, L.; Gastaldini, A.; Vanzin, F.; Veiga, K. Total shrinkage, oxygen permeability, and chloride ion penetration in concrete made with white Portland cement and blast-furnace slag. *Constr. Build. Mater.* **2012**, *37*, 652–659. [CrossRef]

71. *JG/T 337-2011*; Agents of Surface Coating for Protection of Concrete Structures. China Communications Press: Beijing, China, 2011.